RSC Advances

PAPER

View Article Online
View Journal | View Issue

Check for updates

Cite this: *RSC Adv.*, 2022, **12**, 12219

In situ preparation of an anatase/rutile-TiO_2/$Ti_3C_2T_x$ hybrid electrode for durable sodium ion batteries†

Yang Song, Yuchong Kang, Wei Ma * and Haibo Li *

Received 11th March 2022
Accepted 7th April 2022

DOI: 10.1039/d2ra01589g

rsc.li/rsc-advances

Herein, a facile one-step method is developed to *in situ* prepare crystalline anatase and rutile TiO_2 nanocrystals on $Ti_3C_2T_x$ by regulating the metastable Ti ions. The combination of TiO_2 nanocrystals and $Ti_3C_2T_x$ not only introduces extensive accessible sites for Na^+ storage, but also promotes the charge transport by efficiently relieving the collapse of $Ti_3C_2T_x$. Compared with pristine $Ti_3C_2T_x$, the optimized $TiO_2/Ti_3C_2T_x$ hybrid electrode (anatase/rutile-$TiO_2/Ti_3C_2T_x$, A/R-$TiO_2/Ti_3C_2T_x$) exhibits a desirable specific surface area (22.5 $m^2\ g^{-1}$), an ultralow charge transfer resistance (42.46 Ω) and excellent ion diffusion (4.01×10^{-14}). Remarkably, rich oxygen vacancies are produced on $TiO_2/Ti_3C_2T_x$ which is beneficial to enhance the insertion/de-insertion of Na^+ during the charge/discharge process. As a result, the A/R-$TiO_2/Ti_3C_2T_x$ delivers a high average capacity of 205.4 mA h g^{-1} at 100 mA g^{-1} and a desirable capacitance retention rate of 84.7% can be achieved after 600 cycles at 500 mA g^{-1}.

Open Access Article. Published on 22 April 2022. Downloaded on 12/5/2025 2:31:23 PM.
This article is licensed under a Creative Commons Attribution-NonCommercial 3.0 Unported Licence.

1. Introduction

Cost-effective energy storage systems have been one of the most promising candidates to face the challenges of the worldwide energy issues. Among various electrochemical energy storage techniques, the rechargeable lithium-ion batteries (LIBs) and sodium-ion batteries (SIBs) have attracted great interest due to their high energy density and flexible characteristics.[1–4] However, the limited lithium resources increase the fabrication cost, thus hindering the development of LIBs. Compared to LIBs, SIBs have been considered as the most hopeful next-generation secondary battery due to their advantages of abundant sodium reserves.[5,6] Unfortunately, the large diameter of Na^+ (116 pm) is always accompanied by the issues of slow reaction kinetics, low capacity and poor cycle stability when making SIB.[7,8]

MXene, as a newly emerged 2D material, has exhibited prominent advantages, *i.e.* outstanding electronic conductivity and large surface area.[9–11] Essentially, the MXene is proposed as an ideal matrix body to hybridize electrochemical active materials for SIB by inducing a synergistic effect. For example, Lv *et al.* developed $Ti_3C_2T_x$ by intercalation of ethanol or dimethyl sulfoxide. When employed as the anode for SIB, it achieved 110 mA h g^{-1} at a current density of 100 mA g^{-1}, which was 16% higher than that of the original $Ti_3C_2T_x$ (95 mA h g^{-1}).[12] However, due to the easy collapsing characteristics of MXene, the Na^+ storage capacity of the MXene anode is still far away from the theoretical value. To address this issue, various strategies have been proposed to alleviate the structure damage of MXene in the Na^+ storage process. For example, Sun *et al.* provided a surface regulation method, replacing the O-terminal with the PO_2-terminal, which greatly enhanced the specific capacity of Nb_4C_3 MXene and effectively relieves the collapse of MXene.[13] Besides, the preparation of MXene based nanocomposites is also an efficient way to address this issue. The obvious advantage of the nanocomposite is to reduce the volume expansion during charge/discharge and thereby improve the stability of the battery.[14–16] For example, Yang *et al.* *in situ* grew anatase TiO_2 on MXene towards the enlarged spacing layer of MXene. Meanwhile, the anatase TiO_2 nanoparticles also supply additional adsorption sites for sodium ions, which gives rise to a reversible capacity of 52 mA h g^{-1} to 156 mA h g^{-1} with a large current span of 50–2000 mA g^{-1}.[17]

Due to the network structure enabled by the stacking and edge-sharing of TiO_6 octahedra, TiO_2 provides many ideal insertion sites for accommodating Na^+ and the suitable path for the diffusion of Na^+.[18–20] Furthermore, among all kinds of crystalized TiO_2, rutile-TiO_2 exhibits good cycling stability due to its robust structure. Regarding TiO_2, it is known that the TiO_2 anode has the advantages of being non-toxic, low cost, high specific capacity and good rate performance.[21–23] Nevertheless, the large band gap (3.0 eV) associated with TiO_2 causes the inferior electronic conductivity, which brings a negative impact on rate capability.[24,25]

In this work, we aim to construct hybrid structures composed of $Ti_3C_2T_x$ and TiO_2 in different crystallinity for

Ningxia Key Laboratory of Photovoltaic Materials, Ningxia University, Yinchuan, Ningxia, 750021, P. R. China. E-mail: mawei@nxu.edu.cn; lihaibo@nxu.edu.cn

† Electronic supplementary information (ESI) available: The experimental details, XRD patterns, SEM images and cycling performances of A-TiO_2 and R-TiO_2. See https://doi.org/10.1039/d2ra01589g

© 2022 The Author(s). Published by the Royal Society of Chemistry

Open Access Article. Published on 22 April 2022. Downloaded on 12/5/2025 2:31:23 PM.
This article is licensed under a Creative Commons Attribution-NonCommercial 3.0 Unported Licence.

durable SIBs. It is explored that the coupling of TiO_2 with $Ti_3C_2T_x$ not only benefits to support the 2D structure of $Ti_3C_2T_x$, but also introduces additional capacity enabled by TiO_2. Meanwhile, a large number of oxygen vacancies can be generated, which facilitates the insertion/de-insertion of sodium ions. Further, the agglomerate of TiO_2 can be relieved during the preparation. Owing to the synergistic effect, the A/R-TiO_2/$Ti_3C_2T_x$ anode has proved superior Na^+ storage performance.

2. Experimental

2.1 Materials

Ti_3AlC_2 (MAX phase, 325 mesh) powder was purchased from Shanghai Bowei applied material technology Co., Ltd. Hydrofluoric acid (HF-35%), hydrogen peroxide (H_2O_2), Na_2SO_4 and metallic sodium were purchased from Aladdin (China). All reagents are analytically pure and can be used as is without further purification.

2.2 Synthesis of $Ti_3C_2T_x$

1 g Ti_3AlC_2 powder was added into a 100 ml plastic beaker. Meanwhile, 12 ml hydrofluoric acid (HF-35%) was dropped into the beaker under an ice bath environment, and then continuously stirred at 45 °C for 48 hours. After that, the black precipitate was washed repeatedly with deionized water (DI) until it reached a neutral pH value. Finally, it was collected and dried at 60 °C to obtain the $Ti_3C_2T_x$ powder.

2.3 Synthesis of A-TiO_2/$Ti_3C_2T_x$ and A/R-TiO_2/$Ti_3C_2T_x$

0.2 g $Ti_3C_2T_x$ powder, 80 ml DI, 0.5 ml H_2O_2 and 1 ml HCl (36%) were sent into a 100 ml stainless-steel autoclave with Teflon lining and maintained at 110 °C for 12 h. Subsequently, the precipitate was washed repeatedly with DI until the pH equals 7. Afterwards, the product was collected and dried at 60 °C to obtain the A-TiO_2/$Ti_3C_2T_x$. In terms of the synthesis of A/R-TiO_2/$Ti_3C_2T_x$, we followed the same procedure except for setting the reaction at 200 °C.

2.4 Synthesis of A-TiO_2 and A/R-TiO_2

0.2 g $Ti_3C_2T_x$ powder, 80 ml DI, 4 ml H_2O_2 and 1 ml HCl (36%) were sent into a 100 ml stainless-steel autoclave with Teflon lining and maintained at 110 °C for 12 h. Subsequently, the precipitate was washed repeatedly with DI until the pH equals 7. Afterwards, the product was collected and dried at 60 °C to obtain the A-TiO_2. In terms of the synthesis of A/R-TiO_2, we followed the same procedure except for setting the reaction at 200 °C.

2.5 Material characterization

The morphology, structure and elemental distribution were characterized by scanning electron microscopy (SEM, Hitachi SU5000) and transmission electron microscopy (TEM, FEI Talos F-200X). X-ray diffraction (XRD, SmartLab) with Cu Kα radiation at 45 kV and 200 mA over a 2θ range of 5–85° was utilized to examine the internal crystalline structures of samples. The Raman spectra were measured on a spectrometer (DXR, USA) equipped with an optical microscope at room temperature. Various functional groups associated with samples were classified by Fourier transform infrared spectroscopy (FTIR) on a high-resolution infrared spectrometer (WQF-520A). The binding energy of the samples confirmed by X-ray photoelectron spectroscopy (XPS, Thermo ESCALAB 250Xi) was measured using the Al Kα ray ($h\nu$ = 1486.6 kV) with a working voltage of 14.6 kV. The Brunauer–Emmett–Teller (BET) experiment was performed with a surface area analyzer (JW-BK200C). The pore size distribution plot was obtained according to the Barrett–Joyner–Halenda (BJH) method. The oxygen vacancy signal was obtained using a paramagnetic resonance spectrometer (EPR, Emxmicro).

2.6 Electrochemical characterization

The electrochemical behavior and SIB performance of $Ti_3C_2T_x$, A-TiO_2, A/R-TiO_2, A-TiO_2/$Ti_3C_2T_x$ and A/R-TiO_2/$Ti_3C_2T_x$ were studied by making a coin-type battery (CR2032). Initially, the working electrode was prepared by mixing the active materials, superconducting black and polyvinylidene fluoride (PVDF) in *N*-methyl-2-pyrrolidone (NMP) according to a mass ratio of 8 : 1 : 1, and then pasting evenly on copper foam. The average mass loading of the active material was about 2.0 mg cm^{-2}. Subsequently, the battery was assembled in a glove box filled with argon with H_2O and O_2 whose concentrations were below 0.1 and 0.3 ppm, respectively. The constant current charge discharge measurements were performed at room temperature using a battery program-controlled test system (CT2001A, LANHE, China) with a voltage range of 0 to 3 V. The cyclic voltammetry (CV) and electrochemical impedance spectroscopy (EIS) curves were measured using an electrochemical workstation (PARSTAT 3000A-DX, Princeton Applied Research, USA).

3. Results and discussion

3.1 Synthesis and materials characterization

Fig. 1a shows the schematic illustration of the structure of the TiO_2/$Ti_3C_2T_x$ nanocomposite. There are a large number of metastable Ti ions present on both sides of $Ti_3C_2T_x$, which guarantees the building of the TiO_2/$Ti_3C_2T_x$ hybrid.[12,26,27] By regulating the state of metastable Ti ions, the crystallinity of TiO_2 can be rationally controlled. Fig. 1b is the SEM image of $Ti_3C_2T_x$, exhibiting a typical accordion-like layered structure. Fig. 1c shows the SEM image of the A-TiO_2/$Ti_3C_2T_x$ hybrid. Apparently, the accordion-like layered structure remains, while the surface of $Ti_3C_2T_x$ is occupied by a large number of A-TiO_2 nanoparticles. When introducing R-TiO_2 into A-TiO_2/$Ti_3C_2T_x$, as shown in Fig. 1d, regular octahedral nanocrystals have been observed which are deemed as R-TiO_2. Fig. S1† shows the SEM images of A-TiO_2 and A/R-TiO_2, where the TiO_2 particles agglomerate together. The elemental mapping image of A/R-TiO_2/$Ti_3C_2T_x$ in Fig. 1e clearly demonstrates the co-existence of Ti, C and O. Fig. 1f shows the high-resolution transmission electron microscope (HRTEM) image of A/R-TiO_2/$Ti_3C_2T_x$ with the enlarged HRTEM image of the selected area as well. The

© 2022 The Author(s). Published by the Royal Society of Chemistry

Open Access Article. Published on 22 April 2022. Downloaded on 12/5/2025 2:31:23 PM.
This article is licensed under a Creative Commons Attribution-NonCommercial 3.0 Unported Licence.

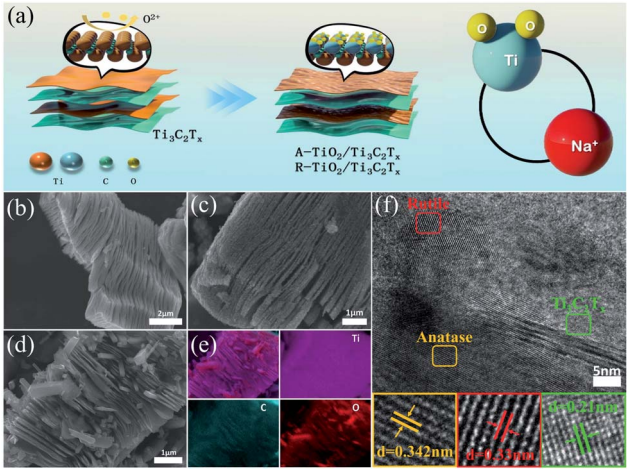

Fig. 1 (a) Schematic illustration of A/R-TiO_2/$Ti_3C_2T_x$, the SEM images of (b) $Ti_3C_2T_x$, (c) A-TiO_2/$Ti_3C_2T_x$, and (d) A/R-TiO_2/$Ti_3C_2T_x$, (e) elemental mapping image of A/R-TiO_2/$Ti_3C_2T_x$, and (f) HRTEM images of A/R-TiO_2/$Ti_3C_2T_x$.

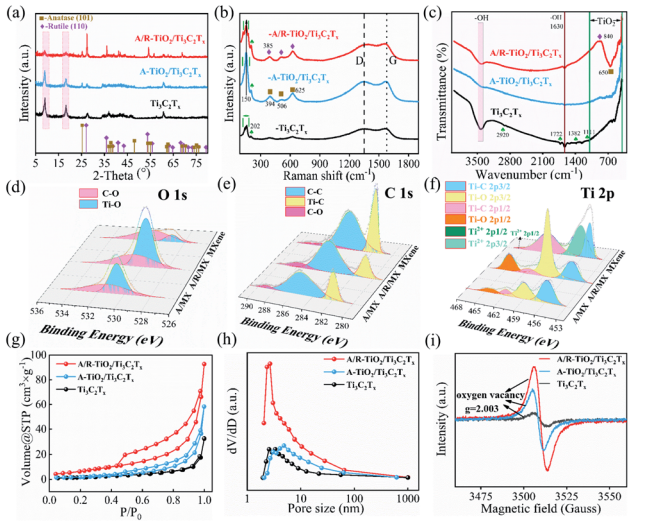

Fig. 2 (a) XRD patterns, (b) Raman spectra, (c) FTIR spectra, (d) O 1s spectra, (e) C 1s spectra, (f) Ti 2p spectra, (g) N_2 adsorption–desorption isotherm, (h) pore size distribution and (i) EPR spectra of $Ti_3C_2T_x$, A-TiO_2/$Ti_3C_2T_x$ and A/R-TiO_2/$Ti_3C_2T_x$.

lattice fringes of d = 0.342 nm, 0.33 nm and 0.21 nm are associated with the (101) plane of A-TiO_2, (110) plane of R-TiO_2 and (105) plane of $Ti_3C_2T_x$, respectively, demonstrating the coexistence of A-TiO_2, R-TiO_2 and $Ti_3C_2T_x$-MXene.[26,28] Consequently, the A/R-TiO_2/$Ti_3C_2T_x$ hybrid is successfully synthesized.

Fig. 2a shows the X-ray diffraction (XRD) patterns of $Ti_3C_2T_x$, A-TiO_2/$Ti_3C_2T_x$ and A/R-TiO_2/$Ti_3C_2T_x$. Basically, the characteristic peaks of $Ti_3C_2T_x$ can be indexed in all samples, particularly two peaks at 9.08° and 18.22°.[29] As a supplementary, the XRD patterns of A-TiO_2 and A/R-TiO_2 are given in Fig. S2.† In terms of the A-TiO_2/$Ti_3C_2T_x$, except for the characteristic peaks of $Ti_3C_2T_x$, a new peak located at 25.31° has emerged, which corresponds to the (101) plane of A-TiO_2. Upon the increase of the oxidation degree, a new peak appearing at 27.2° is assumed as the characteristic peak of the (110) plane of R-TiO_2, proving the presence of the A/R-TiO_2/$Ti_3C_2T_x$ nanocomposite.[25,30,31] By using quantitative full pattern Rietveld refinement from the XRD diffraction patterns of each phase, we have calculated the mass ratio of MXene in TiO_2/MXene nanocomposites, which is 1 : 0.17 for MXene : A-TiO_2 in the A-TiO_2/$Ti_3C_2T_x$ composite and 1 : 1.05 : 4.06 for MXene : A-TiO_2 : R-TiO_2 in A/R-TiO_2/$Ti_3C_2T_x$, respectively.

Fig. 2b and c presents the Raman and Fourier transform infrared spectroscopy (FTIR) spectra of all samples. In the Raman spectrum of $Ti_3C_2T_x$, a distinct peak between 140 cm^{-1} and 160 cm^{-1} refers to the typical C plane and the metastable Ti vibration modes. Besides, Ti–O vibration bands of surface groups arise at 202 cm^{-1}.[32,33] Compared with the Raman spectrum of pristine $Ti_3C_2T_x$, the appearance of strong Ti–O vibration peaks at 625 cm^{-1}, 506 cm^{-1}, 394 cm^{-1} and 150 cm^{-1} in the Raman spectrum of A-TiO_2/$Ti_3C_2T_x$ suggests the existence of A-TiO_2 nanoparticles. Moreover, the shift of the peak from 394 to 385 cm^{-1} and decline of the peak at 150 cm^{-1} in the Raman spectrum of A/R-TiO_2/$Ti_3C_2T_x$ reveal the existence of R-TiO_2 nanoparticles.[34,35] In Fig. 2c, a broad band at 3100 cm^{-1} is ascribed to the stretching vibration of –OH groups that come from the terminations of $Ti_3C_2T_x$, which consist of –OH and –F terminations.[36] The peaks at 1722 cm^{-1} and 2920 cm^{-1} are assigned to C=O and C–H stretching in pristine $Ti_3C_2T_x$, respectively, while bending of the –OH terminal groups of $Ti_3C_2T_x$ contributes to absorption peaks at 1630 cm^{-1} and 584 cm^{-1}. Assignments of the peaks at 1382 cm^{-1} and 1111 cm^{-1} are the C–F vibration and Ti–C–O vibration, respectively.[37] Differing from the FTIR spectrum of $Ti_3C_2T_x$, a strong absorption band emerges from 500 cm^{-1} to 900 cm^{-1} in A-TiO_2/$Ti_3C_2T_x$ due to the existence of A-TiO_2. Remarkably, in A/R-TiO_2/$Ti_3C_2T_x$, the band at 840 cm^{-1} is attributed to the lattice stretching vibration of R-TiO_2 (O–Ti–O). Beyond that, the peak at 650 cm^{-1} would be assigned to the (Ti–O) tensile zone, which is associated with A-TiO_2.[25,38] Based on the above results, we have successfully synthesized the MXene/TiO_2 nanohybrids, in which the crystalinity of TiO_2 can be precisely controlled by regulating the metastable Ti ions through a facile one-step method.

Fig. 2d shows the O 1s spectra of $Ti_3C_2T_x$, A-TiO_2/$Ti_3C_2T_x$ and A/R-TiO_2/$Ti_3C_2T_x$. Apparently, the C–O bond doesn't have a violent change in all samples. In sharp contrast, the Ti–O bond is significantly enhanced in A/R-TiO_2/$Ti_3C_2T_x$, suggesting the presence of a large amount of TiO_2.[14] Fig. 2e gives the C 1s spectra, which can be split into C–C, Ti–C and C–O bonds. The C–C and Ti–C bonds reveal the signature of the Ti–C–Ti structure in all samples. The attenuation of Ti–C peaks in A-TiO_2/$Ti_3C_2T_x$ and A/R-TiO_2/$Ti_3C_2T_x$ is indicative of oxidation of surface Ti ions into TiO_2. In the Ti 2p spectrum (Fig. 2f), one pair of strong peaks located at 456.47 eV and 465.57 eV are correlated with the Ti^{2+}, while two peaks centered at 455.27 eV and 461.27 eV indicate the existence of the Ti–C bond in $Ti_3C_2T_x$.[14,15] There was a controversy; a new pair of peaks occur

Open Access Article. Published on 22 April 2022. Downloaded on 12/5/2025 2:31:23 PM.
This article is licensed under a Creative Commons Attribution-NonCommercial 3.0 Unported Licence.

at about 458.57 and 464.27 eV, which are associated with the Ti–O bonds in A-TiO_2/$Ti_3C_2T_x$ and A/R-TiO_2/$Ti_3C_2T_x$. In addition, the peak areal ratio of Ti–O/Ti–C ($\approx$2.57) in A/R-TiO_2/$Ti_3C_2T_x$ is larger than that of A-TiO_2/$Ti_3C_2T_x$ ($\approx$0.81), demonstrating the presence of a large amount of TiO_2.[8,9,15,32]

Fig. 2g and h show the typical nitrogen adsorption–desorption isotherm and pore size distribution of $Ti_3C_2T_x$, A-TiO_2/$Ti_3C_2T_x$ and A/R-TiO_2/$Ti_3C_2T_x$, respectively. The relatively apparent hysteresis loop is examined on the isotherms of the three samples, implying the mesoporous characteristic. Compared with pure $Ti_3C_2T_x$, the formation of the TiO_2/$Ti_3C_2T_x$ heterojunction structure would bring in larger mesopores, which contributes to larger specific surface area. Incorporation of TiO_2 with different phases into MXene would further reinforce this effect, leading to increased specific surface area.[39,40] Apparently, the N_2 adsorption capacities of the samples follow the order of $Ti_3C_2T_x$ < A-TiO_2/$Ti_3C_2T_x$ < A/R-TiO_2/$Ti_3C_2T_x$. The formation of TiO_2 nanocrystals on MXene provides more adsorption sites for Na ions. Furthermore, we made BET measurements on the three samples, which show that the specific surface area (SSA) of $Ti_3C_2T_x$, A-TiO_2/$Ti_3C_2T_x$ and A/R-TiO_2/$Ti_3C_2T_x$ is 5.0, 6.0 and 22.5 $m^2\ g^{-1}$, respectively. In strong contrast to $Ti_3C_2T_x$ and A-TiO_2/$Ti_3C_2T_x$, the dominant pore size of A/R-TiO_2/$Ti_3C_2T_x$ concentrates on 3–5 nm. The improved SSA with rational pore size makes A/R-TiO_2/$Ti_3C_2T_x$ possess more sodium ion storage sites, which could adapt to strain/stress during cycling and promote electrode/electrolyte contact.[41,42]

Fig. 2i shows the electron paramagnetic resonance (EPR) spectra of $Ti_3C_2T_x$, A-TiO_2/$Ti_3C_2T_x$ and A/R-TiO_2/$Ti_3C_2T_x$. The signal response at 3515 gauss has been observed in all samples, corresponding to a *g* factor of 2.003, which is a characteristic of oxygen vacancies[24] In $Ti_3C_2T_x$, the oxygen vacancies may be related to the surface functional groups. After oxidation, the oxygen vacancies of A-TiO_2/$Ti_3C_2T_x$ have significantly increased, and the signal intensity is about 4.34 times higher than that of $Ti_3C_2T_x$. Additionally, the signal factor of A/R-TiO_2/$Ti_3C_2T_x$ is the strongest among all samples, with ~7.38 times higher signal intensity of $Ti_3C_2T_x$. Notably, oxygen vacancies have been demonstrated to improve the electronic structure, charge transfer, and surface properties of TiO_2 by narrowing the band gap, resulting in the accelerated Na^+ adsorption and diffusion kinetics.[43–45]

3.2 Electrochemical performance and ion diffusion kinetics

The cycling performances of the $Ti_3C_2T_x$, A-TiO_2/$Ti_3C_2T_x$ and A/R-TiO_2/$Ti_3C_2T_x$ electrodes at 100 mA g^{-1} are exhibited in Fig. 3a. The three electrodes realize good cycling stability. Remarkably, the A/R-TiO_2/$Ti_3C_2T_x$ electrode delivers a reversible capacity of 183.5 mA h g^{-1} after 100 cycles, while the reversible capacities of $Ti_3C_2T_x$ and A-TiO_2/$Ti_3C_2T_x$ separately are only 96.8 and 107.9 mA h g^{-1}. As a comparison, Fig. S3† shows the reversible capacities of A-TiO_2 and A/R-TiO_2 after 100 cycles, which are 55.6 and 118.7 mA h g^{-1}, respectively. Both are far less than the capacity of the A/R-TiO_2/$Ti_3C_2T_x$ anode. Further, Fig. 3b shows that the rate capacities of the A/R-TiO_2/$Ti_3C_2T_x$ electrode are 205.4, 135.7, 103.5, 77.5 and 40.6 mA h g^{-1} at 100, 500, 1000, 2000 and 5000 mA g^{-1}. These values are considerably higher than those for the A-TiO_2/$Ti_3C_2T_x$ and $Ti_3C_2T_x$ electrodes, which are 132.4 mA h g^{-1}, 78.3 mA h g^{-1}, 50.1 mA h g^{-1}, 25.6 mA h g^{-1}, and 11.4 mA h g^{-1} and 109.9 mA h g^{-1}, 59.7 mA h g^{-1}, 31.1 mA h g^{-1}, 11.4 mA h g^{-1}, and 12.6 mA h g^{-1}, respectively. Fig. 3c displays the first four continued CV curves of the A/R-TiO_2/$Ti_3C_2T_x$ with potential windows of 0.01–3.0 V at 0.1 mV s^{-1}. As illustrated, the irreversible oxidation peak in the anodic process for the first cycle can be ascribed to the decomposition of the electrolyte, the formation of the solid electrolyte interface (SEI), or the irreversible muti-electrochemical reactions.[46] In the case of the first sodiation process, two broad anodic peaks occurred at 1.39 V and 2.03 V, respectively, and their intensity decreased compared with the subsequent cycles, corresponding to the extraction of sodium ions from the $Ti_3C_2T_x$ electrode. No significant shift was observed in subsequent cycles, suggesting that the charge storage in $Ti_3C_2T_x$ was due to the intercalation of Na^+ rather than a conversion reaction.[12,14] In the following three subsequent cycles, a cathodic peak near 2.35 V can be clearly observed due to the sodiation, while an anodic peak near 0.45 V is attributed to the de-sodiation. This reversible process is accompanied by the conversion of Ti^{4+}/Ti^{3+} couples in the A/R-TiO_2/$Ti_3C_2T_x$.[14,17,46] Beyond the first cycle, the subsequent cycles are almost overlapping, implying the high reversibility of the electrode. The selected charge–discharge curves of A/R-TiO_2/$Ti_3C_2T_x$ within 0–3.0 V at a current density of 100 mA g^{-1} are drawn in Fig. 3d. The initial discharge and charge capacity were 774.7 and 270.9 mA h g^{-1}, respectively, delivering a Coulomb efficiency (CE) of 35%. The low CE and huge irreversible capacity loss are mainly resulted from the formation of SEI film and irreversible electrochemical reaction.[16,47] Interestingly, the charge–discharge curves after the first cycles are going to overlap, suggesting the improved reversibility of the A/R-TiO_2/

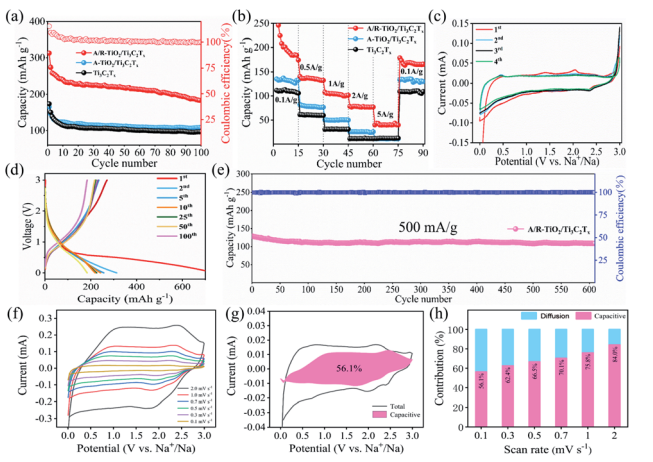

Fig. 3 (a) Cycling performances at 100 mA g^{-1} and (b) rate capabilities of $Ti_3C_2T_x$, A-TiO_2/$Ti_3C_2T_x$ and A/R-TiO_2/$Ti_3C_2T_x$, (c) CV curve of A/R-TiO_2/$Ti_3C_2T_x$, (d) GCD curves at 100 mA g^{-1} and (e) cycling performances at 500 mA g^{-1}, (f) CV curves of A/R-TiO_2/$Ti_3C_2T_x$ at scan rates ranging from 0.1 to 2.0 mV s^{-1}, and (g) and (h) the capacitive contribution of A/R-TiO_2/$Ti_3C_2T_x$ at 0.1 mV s^{-1}, normalized contribution ratios of capacitive and diffusion-controlled capacity of A/R-TiO_2/$Ti_3C_2T_x$ at different scan rates.

© 2022 The Author(s). Published by the Royal Society of Chemistry

Open Access Article. Published on 22 April 2022. Downloaded on 12/5/2025 2:31:23 PM.
This article is licensed under a Creative Commons Attribution-NonCommercial 3.0 Unported Licence.

$Ti_3C_2T_x$ electrode. Fig. 3e illustrates the long cycling performance of A/R-TiO_2/$Ti_3C_2T_x$ at 500 mA g^{-1} in 600 cycles. Essentially, the reversible initial and final capacities are 128.8 and 109.1 mA h g^{-1}, respectively, deducing a capacitance retention rate of 84.7%.

To figure out the charge-storage mechanism of the A/R-TiO_2/$Ti_3C_2T_x$ electrode, cyclic voltammetry (CV) profiles at various scan rates were tested. Fig. 3e illustrates the CV curves of A/R-TiO_2/$Ti_3C_2T_x$ at scan rates of 0.1, 0.3, 0.5, 0.7, 1.0 and 2.0 mV s^{-1}, respectively. Classically, the charge-storage mechanism can be investigated by exploring the relationship between the peak current (i, mA) and the scan rates (v, mV s^{-1}):

$$i = av^b \quad (1)$$

$$\log(i) = b\log(v) + \log(a) \quad (2)$$

where a and b are adjustable parameters. When b equals 1, the capacity is fully governed by the capacitive-controlled process; if b equals 0.5, it corresponds to a diffusion-controlled process. Fig. S4† shows that the b values of A/R-TiO_2/$Ti_3C_2T_x$ are 0.888 and 0.910, which realizes the mixed behavior of diffusion-controlled and capacitive-controlled process. Further, the ratio of contribution of capacitive-controlled process and diffusion-controlled process can be quantitatively estimated through the following equations:

$$i(v) = k_1v + k_2v^{1/2} \quad (3)$$

$$i(v)/v^{1/2} = k_1v^{1/2} + k_2 \quad (4)$$

where $i(v)$, k_1v, $k_2v^{1/2}$ and v denote the current at a fixed potential, the capacitive-controlled current, the diffusion-controlled current and the scan rate, respectively. The capacitance contribution of the capacitive-controlled process at a given scan rate can be figured out by obtaining k_1. Through linear fittings of the $v^{1/2}$ *vs.* $i/v^{1/2}$ plots, k_1 values at different scan rates are determined.[48] As shown in Fig. 3g and h, as the scan rate increased from 0.1 mV s^{-1} to 2 mV s^{-1}, the capacitive contribution grew from 56.1% to 84.0% of the total stored charge, which implies that the electrochemical process is determined by both intercalation and capacitive reactions and the capacitive charge storage contributes most to the total capacity at high rates.

Fig. 4a shows the Nyquist plot and equivalent circuit diagrams of the three electrodes at a frequency of 0.01 to 10^6 Hz. As shown in Fig. 4a, all plots exhibit similar shapes composed of a straight line in the low frequency area and a semicircle in the high frequency range.[49] The equivalent circuit is given in the inset, where R_s, R_{ct} and W_0 represent the electrolyte resistance, the interfacial charge transfer resistance and the Warburg impedance related to the Na^+ diffusion within the electrode.[50] As shown in Table 1, R_{ct} significantly decreases when TiO_2 is incorporated in $Ti_3C_2T_x$ regardless of the crystal type. This can be attributed to the improved conductivity and increased electroactive sites. Moreover, the R_{ct} of A/R-TiO_2/$Ti_3C_2T_x$ is 42.46 Ω, which is much lower than that of A-TiO_2/$Ti_3C_2T_x$ (119 Ω), indicating the high interfacial charge transfer which is beneficial to

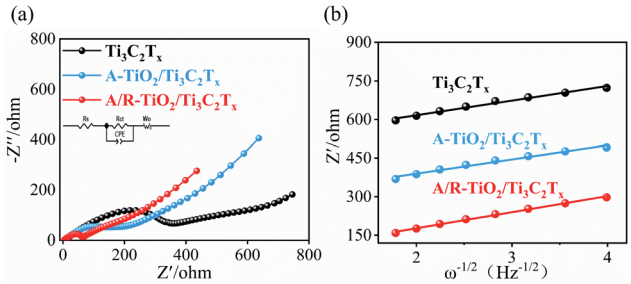

Fig. 4 (a) EIS spectra and Nyquist plots, and (b) relationship between Z' and $\omega^{-1/2}$ at low frequencies.

Table 1 The charge transfer impedance, weber factor and diffusion coefficient of $Ti_3C_2T_x$, A-TiO_2/$Ti_3C_2T_x$ and A/R-TiO_2/$Ti_3C_2T_x$

Electrode	R_{ct}/Ω	σ/ohm cm^2 $s^{-0.5}$	D_{Na^+}/cm^2 s^{-1}
$Ti_3C_2T_x$	289.8	57	2.858×10^{-15}
A-TiO_2/$Ti_3C_2T_x$	119	55.1	8.602×10^{-15}
A/R-TiO_2/$Ti_3C_2T_x$	42.46	48	4.01×10^{-14}

enhance the rate capability. Except for the resistance, we calculated the diffusion coefficient of sodium ions (D_{Na^+}) from the low frequency domain, which can be expressed by the following equations:

$$D = \frac{R^2T^2}{2A^2n^4F^4C^2\sigma^2} \quad (5)$$

$$Z' = R_e + R_{ct} + \sigma\omega^{1/2} \quad (6)$$

R denotes the molar gas constant (8.314 J K^{-1} mol^{-1}), T is the absolute temperature (298.15 K), A is the area of the electrode, n

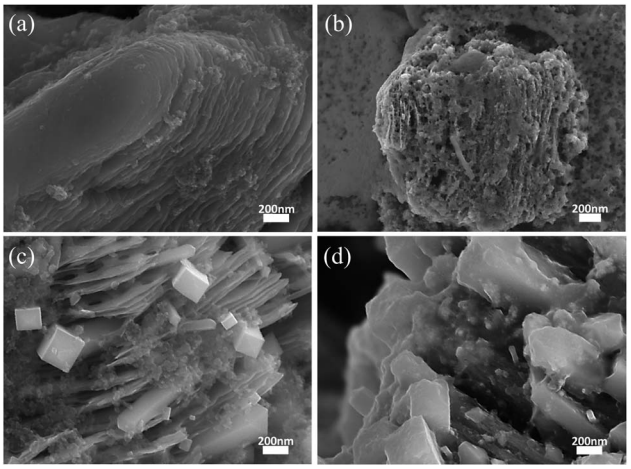

Fig. 5 SEM images of (a and b) the pure $Ti_3C_2T_x$ and (c and d) A/R-TiO_2/$Ti_3C_2T_x$ electrode before/after 100 charging–discharging cycles, respectively.

Open Access Article. Published on 22 April 2022. Downloaded on 12/5/2025 2:31:23 PM.
This article is licensed under a Creative Commons Attribution-NonCommercial 3.0 Unported Licence.

is the number of electrons transferred during the reaction, C is the sodium ion concentration and F is the Faraday constant (96 486 C mol^{-1}). Fig. 4b shows the relationship between Z' and $\omega^{-1/2}$ at low frequencies.[32] The values of σ and the D_{Na^+} are summarized in Table 1. The D_{Na^+} of A/R-TiO_2/$Ti_3C_2T_x$ is 4.01 × 10^{-14} cm^2 s^{-1} which is approximately 14.01 times and 4.66 times higher than the D_{Na^+} of $Ti_3C_2T_x$ (2.858 × 10^{-15} cm^2 s^{-1}) and A-TiO_2/$Ti_3C_2T_x$ (8.602 × 10^{-15} cm^2 s^{-1}), respectively. This is presumably ascribed to the incorporation of long rod-like R-TiO_2 nanocrystals, which can effectively relieve the collapse of $Ti_3C_2T_x$ layers.

Fig. 5a and b show the SEM images of the $Ti_3C_2T_x$ electrode before and after the cycling, respectively. Obviously, the layered structure of pure $Ti_3C_2T_x$ seriously collapsed after cycling. In sharp contrast, the structure of A/R-TiO_2/$Ti_3C_2T_x$ remains largely unaffected (Fig. 5c and d), illustrating its desirable stability.

4. Conclusions

Through the surface regulation of $Ti_3C_2T_x$, we generated A-TiO_2 and R-TiO_2 *in situ* from metastable Ti ions on the surface of $Ti_3C_2T_x$ by a one-step method to obtain nano hybrid structures. The growth of crystalline A-TiO_2 and R-TiO_2 is beneficial to improve the collapse of $Ti_3C_2T_x$. The 2D structure can provide a fast channel for the transmission of Na^+. A-TiO_2 and R-TiO_2 crystals can introduce more active sites for Na^+. Moreover, the crystals can provide a supporting effect for the layered structure and maintain the integrity and firmness of the structure. Meanwhile, a large number of oxygen vacancies can be introduced into the composite which are conducive to the insertion and extraction of Na^+. Due to the advantages of the A/R-TiO_2/$Ti_3C_2T_x$ hybrid structure, the prepared A/R-TiO_2/$Ti_3C_2T_x$ electrode has proved high capacity, great rate performance and long-term cycle stability. We believe that these findings will provide new ideas for the design of nanostructured electrodes for advanced rechargeable batteries.

Conflicts of interest

There are no conflicts to declare.

Acknowledgements

This work was supported by the National Natural Science Foundations of China (NSFC11704207) and project of Ningxia key R&D plan (2021BEE03006).

References

1 K. Chayambuka, G. Mulder, D. L. Danilov and P. H. L. Notten, *Adv. Energy Mater.*, 2020, **10**, 2001310.
2 Y. R. Lim, F. Shojaei, K. Park, C. S. Jung, J. Park, W. I. Cho and H. S. Kang, *Nanoscale*, 2018, **10**, 7047–7057.
3 L. Sun, J. Xie, X. Zhang, L. Zhang, J. Wu, R. Shao, R. Jiang and Z. Jin, *Nanoscale*, 2020, **49**, 15712–15717.
4 F. Yang, F. Yu, Z. Zhang, K. Zhang, Y. Lai and J. Li, *Chem.–Eur. J.*, 2016, **22**, 2333–2338.
5 J. Zhu, J. Roscow, S. Chandrasekaran, L. Deng, P. Zhang, T. He, K. Wang and L. Huang, *ChemSusChem*, 2020, **13**, 1275–1295.
6 K.-H. Nam, K.-J. Jeon and C.-M. Park, *Energy Storage Mater.*, 2019, **17**, 78–87.
7 Y. Zhang, N. Wang and Z. Bai, *Appl. Sci.*, 2020, **10**, 3098.
8 J. Lee, J. K. Lee, K. Y. Chung, H.-G. Jung, H. Kim, J. Mun and W. Choi, *Electrochim. Acta*, 2016, **200**, 21–28.
9 P. Ma, D. Fang, Y. Liu, Y. Shang, Y. Shi and H. Y. Yang, *Adv. Sci.*, 2021, **8**, 2003185.
10 J. Li, C. Guo and C. M. Li, *ChemSusChem*, 2020, **13**, 1047–1070.
11 A. VahidMohammadi, W. Liang, M. Mojtabavi and M. Wanunu, *Energy Storage Mater.*, 2021, **41**, 554–562.
12 G. Lv, J. Wang, Z. Shi and L. Fan, *Mater. Lett.*, 2018, **219**, 45–50.
13 B. Sun, Q. Lu, K. Chen, W. Zheng, Z. Liao, N. Lopatik, D. Li, M. Hantusch, S. Zhou, H. I. Wang, Z. Sofer, E. Brunner, E. Zschech, M. Bonn, R. Dronskowski, D. Mikhailova, Q. Liu, D. Zhang, M. Yu and X. Feng, *Adv. Mater.*, 2022, **e2108682**, 1–11.
14 P. Wang, X. Lu, Y. Boyjoo, X. Wei, Y. Zhang, D. Guo, S. Sun and J. Liu, *J. Power Sources*, 2020, **451**, 227756.
15 Z. Yuan, Y. Fan, Y. Chen, X. Liu, B. Liu and S. Han, *Int. J. Hydrogen Energy*, 2020, **45**, 21666–21675.
16 L. Wang, X. Zhang, Y. Xu, C. Li, W. Liu, S. Yi, K. Wang, X. Sun, Z. S. Wu and Y. Ma, *Adv. Funct. Mater.*, 2021, **31**, 2104286.
17 C. Yang, Y. Liu, X. Sun, Y. Zhang, L. Hou, Q. Zhang and C. Yuan, *Electrochim. Acta*, 2018, **271**, 165–172.
18 Y. Zhang, X. Pu, Y. Yang, Y. Zhu, H. Hou, M. Jing, X. Yang, J. Chen and X. Ji, *Phys. Chem. Chem. Phys.*, 2015, **17**, 15764–15770.
19 H. Usui, Y. Domi, T. H. Nguyen, Y. Tanaka and H. Sakaguchi, *ACS Omega*, 2020, **5**, 15495–15501.
20 Z. Hong, K. Zhou, J. Zhang, Z. Huang and M. Wei, *J. Mater. Chem. A*, 2015, **3**, 17412–17416.
21 G. Zou, J. Chen, Y. Zhang, C. Wang, Z. Huang, S. Li, H. Liao, J. Wang and X. Ji, *J. Power Sources*, 2016, **325**, 25–34.
22 E. Ventosa, B. Mei, W. Xia, M. Muhler and W. Schuhmann, *ChemSusChem*, 2013, **6**, 1312–1315.
23 E. Ventosa, A. Tymoczko, K. Xie, W. Xia, M. Muhler and W. Schuhmann, *ChemSusChem*, 2014, **7**, 2584–2589.
24 H. He, D. Sun, Q. Zhang, F. Fu, Y. Tang, J. Guo, M. Shao and H. Wang, *ACS Appl. Mater. Interfaces*, 2017, **9**, 6093–6103.
25 H. He, D. Huang, W. Pang, D. Sun, Q. Wang, Y. Tang, X. Ji, Z. Guo and H. Wang, *Adv. Mater.*, 2018, **30**, 1801013.
26 A. A. Khan and M. Tahir, *Appl. Catal., B*, 2021, **285**, 119777.
27 S. Elumalai, M. Yoshimura and M. Ogawa, *Chem.–Asian J.*, 2020, **15**, 1044–1051.
28 Y. Fang, B. Tan, Q. Chen, X. Ao and Y. Cao, *J. Colloid Interface Sci.*, 2021, **601**, 581–593.
29 T. Huang, Y. Jiang, G. Shen and D. Chen, *ChemSusChem*, 2020, **13**, 1093–1113.

© 2022 The Author(s). Published by the Royal Society of Chemistry

Open Access Article. Published on 22 April 2022. Downloaded on 12/5/2025 2:31:23 PM.
This article is licensed under a Creative Commons Attribution-NonCommercial 3.0 Unported Licence.

30 N. Radić, B. Grbić, S. Petrović, S. Stojadinović, N. Tadić and P. Stefanov, *Phys. B*, 2020, **599**, 412544.
31 L. N. Quan, Y. H. Jang, Y. J. Jang, J. Kim, W. Lee, J. H. Moon and D. H. Kim, *ChemSusChem*, 2014, **7**, 2590–2596.
32 H. Zhang, L. Yang, P. Zhang, C. Lu, D. Sha, B. Yan, W. He, M. Zhou, W. Zhang, L. Pan and Z. Sun, *Adv. Mater.*, 2021, **33**, 2008447.
33 T. Hu, J. Wang, H. Zhang, Z. Li, M. Hu and X. Wang, *Phys. Chem. Chem. Phys.*, 2015, **17**, 9997–10003.
34 S. A. Bhandarkar, Prathvi, A. Kompa, M. S. Murari, D. Kekuda and R. K. Mohan, *Opt. Mater.*, 2021, **118**, 111254.
35 Prathvi, S. A. Bhandarkar, A. Kompa, D. Kekuda, M. M. S. Murari, M. P. Telenkov, K. K. Nagaraja and K. Mohan Rao, *Surf. Interfaces*, 2021, **23**, 100910.
36 M. Naguib, M. Kurtoglu, V. Presser, J. Lu, J. Niu, M. Heon, L. Hultman, Y. Gogotsi and M. W. Barsoum, *Adv. Mater.*, 2011, **23**, 4248–4253.
37 Z. Shen, W. Chen, H. Xu, W. Yang, Q. Kong, A. Wang, M. Ding and J. Shang, *Int. Res. J. Publ. Environ. Health*, 2019, **16**, 4659.
38 N. Malesic Eleftheriadou, A. Ofrydopoulou, M. Papageorgiou and D. Lambropoulou, *Appl. Sci.*, 2020, **10**, 2368.
39 P. Gao, H. Shi, T. Ma, S. Liang, Y. Xia, Z. Xu, S. Wang, C. Min and L. Liu, *ACS Appl. Mater. Interfaces*, 2021, **13**, 51028–51038.
40 L. Wang, J. Ren, Q. Gong, J. Xuan, M. Sun, H. Zhang, Q. Zhang, G. Yin and B. Liu, *J. Mater. Sci.*, 2022, **57**, 5396–5409.
41 R. B. Ambade, G. K. Veerasubramani, S. B. Ambade, M. Christy, W. Eom, H. Shin, Y.-B. Kim, D.-W. Kim and T. H. Han, *Carbon*, 2021, **178**, 332–344.
42 Z. Sun, Z. Zhang and H. Li, *Mater. Lett.*, 2021, **303**, 130570.
43 Y. Zhang, Z. Ding, C. W. Foster, C. E. Banks, X. Qiu and X. Ji, *Adv. Funct. Mater.*, 2017, **27**, 1700856.
44 L. Huang, L. Zeng, J. Zhu, L. Sun, L. Yao, L. Deng and P. Zhang, *J. Power Sources*, 2021, **493**, 229678.
45 Q. Wang, S. Zhang, H. He, C. Xie, Y. Tang, C. He, M. Shao and H. Wang, *Chem.–Asian J.*, 2021, **16**, 3–19.
46 Y. Li, C. Chen, M. Wang, W. Li, Y. Wang, L. Jiao and H. Yuan, *J. Power Sources*, 2017, **361**, 326–333.
47 Z. Zhang, Y. Du and H. Li, *Nanotechnology*, 2020, **31**, 095402.
48 X. Zhao, W. Wang, Z. Hou, X. Fan, G. Wei, Y. Yu, Q. Di, Y. Liu, Z. Quan and J. Zhang, *Inorg. Chem. Front.*, 2019, **6**, 562–565.
49 G. Ma, H. Shao, J. Xu, Y. Liu, Q. Huang, P. L. Taberna, P. Simon and Z. Lin, *Nat. Commun.*, 2021, **12**, 5085.
50 A. Henry, N. Louvain, O. Fontaine, L. Stievano, L. Monconduit and B. Boury, *ChemSusChem*, 2016, **9**, 264–273.

© 2022 The Author(s). Published by the Royal Society of Chemistry